



Engineering the low-coordinated single cobalt atom to boost persulfate activation for enhanced organic pollutant oxidation

Xiaoying Liang¹, Di Wang¹, Zhiyu Zhao, Tong Li, Zhenhuan Chen, Yaowen Gao^{*}, Chun Hu

Institute of Environmental Research at Greater Bay, Key Laboratory for Water Quality and Conservation of the Pearl River Delta, Ministry of Education, Guangzhou University, Guangzhou 510006, China



ARTICLE INFO

Keywords:

Single-atom catalysts
Coordination number
Electron density
Persulfate conversion
Active radicals

ABSTRACT

Two atomically dispersed cobalt catalysts with different nitrogen coordination numbers (denoted as $\text{Co}_{\text{SA}}\text{-N}_x\text{-C}$) were synthesized and firstly compared to activate peroxydisulfate (PDS) for bisphenol A (BPA) degradation. Theoretical calculations unveiled that lowering the Co—N coordination number from four to three can apparently increase the electron density of the single Co atom in $\text{Co}_{\text{SA}}\text{-N}_3\text{-C}$ to enhance PDS conversion. The low-coordinated $\text{Co}_{\text{SA}}\text{-N}_3\text{-C}$ with Co—N₃ coordination structure displays a high specific activity of $0.067 \text{ L min}^{-1} \text{ m}^{-2}$, which is 1.31 times greater than that of $\text{Co}_{\text{SA}}\text{-N}_4\text{-C}$ with normal Co—N₄ configuration ($0.051 \text{ L min}^{-1} \text{ m}^{-2}$) in PDS activation. Electron paramagnetic resonance (EPR) measurements and quenching tests confirmed the primary role of sulfate radical ($\text{SO}_4^{\bullet-}$) in BPA oxidation over $\text{Co}_{\text{SA}}\text{-N}_3\text{-C}$ with PDS. Moreover, $\text{Co}_{\text{SA}}\text{-N}_3\text{-C}$ delivers favorable durability for PDS activation and potential practicability for realistic wastewater remediation. These findings provide a novel and useful avenue to coordination number modulation of SACs for wider environmental applications.

1. Introduction

As a representative precursor of sulfate radical ($\text{SO}_4^{\bullet-}$) and hydroxyl radical ($\bullet\text{OH}$), persulfate has been widely applied as a promising oxidant in advanced oxidation of aqueous recalcitrant organic contaminants [1–4]. Among various activators, transition metal ions appear to be most effective for persulfate activation, but they suffer from poor stability and recyclability [5,6]. Heterogeneous catalysts, particularly transition metal oxides [7–11] and their supported ones [12–15], can surmount these issues; however, the sluggish kinetics and inhomogeneity of active centers greatly restrict the utilization efficiency of reactive surface metallic atoms, resulting in unsatisfactory catalytic performance. Very currently, a kind of heterogeneous catalysts with atomic dispersion of isolated metal sites on appropriate supports, defined as single-atom catalysts (SACs) [16], can connect the advantages of homogeneous and heterogeneous catalysts [17,18]. With atomically dispersed metal atoms being as robust active centers, SACs can achieve maximized atom usage and deliver excellent catalytic activities in heterogeneous catalysis, including environmental catalysis such as persulfate-based catalytic oxidation reaction [19,20].

Carbon-based materials are extensively used as metal-free supports

in the preparation of SACs because of their abundance, high porosity and electron mobility, and tunable surface structure [21]. Nitrogen (N) doping is widely exploited to enhance the interaction of metal (M) atoms with carbon substrates via the formation of strong M—N bonds [22]. For instance, Li et al. [23] reported the utilization of N-doped graphene derived from bimetallic Prussian blue analogue to anchor single Co atom for the formation of atomically dispersed Co—N₄ sites via coordination of a Co atom with surrounding four N atoms, which were responsible for peroxymonosulfate (PMS) activation to produce singlet oxygen (${}^1\text{O}_2$) toward organic pollutant oxidation. Afterwards, multiple carbon-based SACs with atomic dispersion of Co [24,25], Fe [26–29], and Mn [30] atoms on a variety of carbon substrates have been synthesized and implemented to activate PMS, where four nitrogen atoms coordinated metal atoms, namely M—N₄ moieties, served as active centers for PMS conversion. In spite of similar single-atomic M—N₄ structure, the carbon-based SACs encompassing diverse metal atoms (Fe, Co, Mn, etc.) exhibited rather different catalytic activities in the conversion of PMS with controversial PMS activation mechanisms including radical and non-radical pathways. This may be attributable to the electronic metal-support interactions since the diverse metal atoms with disparate electronegativities could regulate the local electronic structures or spin

* Corresponding author.

E-mail address: gaoyw@gzhu.edu.cn (Y. Gao).

¹ X.Y.L. and D.W. contributed equally to this work.

states of M—N₄ moieties in these carbon-based SACs [31], which significantly affected the interaction between PMS and active centers and hence differed the catalytic performance of SACs in PMS activation.

In addition to alteration of metal atoms, adjustment of coordination number x (M—N_x) is another appealing approach to modulate both geometric and electronic architectures of carbon-based SACs, which can observably tune catalytic property of active sites and thus further optimize catalytic performance of the specific SACs [17]. A recent work demonstrated that single-atom cobalt catalysts derived from metal-organic frameworks (MOFs) with lower coordination number delivered much higher electrocatalytic activity for carbon dioxide (CO₂) reduction [32]. The similar electrocatalytic CO₂ reduction selectivity enhancement was also achieved on the MOFs-derived single-atom Ni catalysts, where the low-coordinated Ni-N₃-C catalyst presented much superior performance for CO₂ electroreduction in comparison with the Ni-N₄-C counterpart [33]. Taking inspiration from the regulation of coordination number on single-atom Co and Ni catalysts for electrocatalytic conversion reaction, it is highly reasonable to anticipate that engineering the low-coordinated single Co atom can facilitate persulfate activation on single-atom Co catalysts, however, the relevant study seems to be sparse. On the other hand, the previous persulfate activation over SACs mainly focused on PMS conversion due to the asymmetric molecular structure of PMS (HO—SO₃[−]), which renders it easier to be activated than peroxydisulfate (PDS, O₃S—O—O—SO₃[−]) with a symmetric structure [2,34,35]. However, PDS is much more affordable for in situ remediation (0.74 USD kg^{−1}) in comparison to PMS (2.20 USD kg^{−1}) [2]. Moreover, PDS possesses higher solubility and stability than PMS, and meanwhile, PDS with the same concentration causes less solution pH decrease as compared to PMS [3,36]. These above characters suggest that PDS seems to be more suitable for large-scale applications. Nonetheless, there have been no reports to experimentally explore the application of single-atom Co catalysts in the activation of PDS.

Herein, we demonstrate a cascade-protection strategy to synthesize single-atomic Co—N_x sites on N-doped porous carbon with disparate coordination numbers via varying the pyrolysis temperature to control nitrogen release. Two atomically dispersed Co sites with four- and three-coordinated nitrogen atoms can be selectively fabricated at 800 and 900 °C and designated as Co_{SA}-N₄-C and Co_{SA}-N₃-C, respectively. As a persulfate activator, the Co_{SA}-N₃-C catalyst exhibits superior catalytic performance in PDS conversion, with its specific catalytic activity (normalizing organic contaminant degradation rate constant toward specific surface area and loading of a catalyst) significantly higher than that of Co_{SA}-N₄-C and the Co nanoparticles supported on N-doped carbon (Co-N-C). Theoretical calculations manifested that lowering the coordination number can increase the electron density of single Co atom in the active Co—N₃ center to facilitate PDS adsorption and successive conversion, thereby boosting the generation of active radicals, which accounts for the superior specific activity of Co_{SA}-N₃-C to that of Co_{SA}-N₄-C. Moreover, the Co_{SA}-N₃-C catalyst delivers favorable stability in PDS activation and potential applicability in practical industrial wastewater purification. This work offers a valuable route to design high-performance SACs via coordination microenvironment modulation for environmental applications.

2. Experimental section

2.1. Chemicals

Sodium citrate (99%), 5,5-dimethyl-1-pyrroline N-oxide (DMPO), acid orange 7, cobalt nitrate hexahydrate ($\geq 98\%$), melamine (99%), methanol (99%), sodium persulfate ($\geq 98\%$), bisphenol A ($\geq 98\%$), sulfamethoxazole, furfuryl alcohol, 2-chlorophenol (99%), 1,10-phenanthroline (99%), and *tert*-butyl alcohol ($\geq 99.5\%$) were purchased from Adamas Reagent Co., Ltd. Glucose was obtained from TCI (Shanghai) Chemical Industry Development Co., Ltd. Other reagents were commercially available and used as received.

2.2. Synthesis procedure

The single-atom cobalt catalysts were synthesized according to our previous work [26] but with some modifications. Specifically, sodium citrate was carbonized at 800 °C to serve as carbon support (denoted as CS). Subsequently, the CS, glucose, and cobalt nitrate hexahydrate with the weight ratio of 100:10:1 were ultrasonically dispersed in ultrapure water for 30 min. The solid was rinsed with ultrapure water, dried overnight in an oven at 60 °C, and then grinded together with melamine at a mass ratio of 1:6. On account of nitrogen release at elevated temperature, the resultant powder was calcined for 3 h at 900 °C in a conventional tube furnace with Ar circumstance to acquire the low-coordinate single-atom cobalt catalyst (marked as Co_{SA}-N₃-C), while the atomically dispersed cobalt catalyst with coordination number of four (named as Co_{SA}-N₄-C) was obtained at the pyrolysis temperature of 800 °C. For a better comparison, the Co nanoparticles supported on N-doped carbon (marked as Co-N-C) and nitrogen-doped carbon support (N-C) were also prepared in parallel to that of Co_{SA}-N₃-C except for no addition of glucose and cobalt source, respectively.

2.3. Characterizations

X-ray diffraction (XRD) patterns of samples were recorded on Bruker D8 diffractometer under Cu K α radiation ($\lambda = 1.5418 \text{ \AA}$). The morphology and microstructure were characterized with scanning electron microscopy (SEM, Quanta FEG 250) and transmission electron microscopy (TEM, Tecnai G2 F20). Atomic dispersion of metal atoms were observed with a double spherical aberration corrected scanning TEM (STEM, JEOL JEM-ARM200F). The chemical environments of samples were measured by X-ray photoelectron spectroscopy (XPS, Escalab 250Xi). The specific surface area was tested with the Brunauer-Emmett-Teller method (Micrometrics ASAP 2460). Raman spectra were obtained using a Horiba LabRAM HR Evolution Raman spectrometer with a 532 nm laser. The inductively coupled plasma optical emission spectrometry (ICP-OES) measurements were undertaken on Avio 200, PerkinElmer. Electrochemical impedance spectroscopy (EIS) analysis was performed on a CHI 700E electrochemical workstation using a standard three-electrode cell system under the frequency range from 1 Hz to 100 kHz with 5 mV amplitude. The as-prepared Co_{SA}-N_x-C, Pt foil, and Ag/AgCl electrode were utilized as working electrode, counter electrode, and reference electrode, respectively. The X-ray absorption fine structure (XAFS) spectroscopy experiments were carried out in transmission mode at beam line 14W1B of the Shanghai Synchrotron Radiation Facility (SSRF). Data processing of the XANES and EXAFS spectra were performed using the IFEFFIT package.

2.4. Persulfate activation and analyses

The persulfate activation performance was evaluated through bisphenol A (BPA) degradation, which was conducted in 30 mL BPA solution (50 μM) at 30 °C, followed by the addition of PDS (2 mM) and catalyst (0.05 g L^{−1}) under magnetic stirring. The reaction solutions were regularly sampled (1 mL of the suspension was withdrawn every minute during the reaction), and filtered through 0.22 μm nylon membranes for analysis. The concentration of BPA was detected via an Agilent 1260 Infinity high-performance liquid chromatography using a Poroshell 120 EC-C18 column (4.6 \times 100 mm, 2.7 μm). The mixture consisting of methanol and water in the ratio of 70:30 (v/v) was utilized as the mobile phase with the flowing rate of 1 mL min^{−1}, and the detection wavelength was set to be 225 nm. The mobile phases for 2-chlorophenol (2-CP) and sulfamethoxazole (SMZ) were comprised of methanol and water in the ratio of 60:40 (v/v) and 55:45 (v/v), with detection wavelengths of 275 nm and 226 nm, respectively. The concentration of acid orange 7 (AO7) was measured via a UV-vis spectrometer (752 N, INESA) at 485 nm. The amount of cobalt ions leaching from the catalyst after catalytic reaction was measured by ICP-OES (Avio

200, PerkinElmer). The residual total organic carbon (TOC) was measured by a Shimadzu TOC-L instrument. The stability of $\text{Co}_{\text{SA}}\text{-N}_3\text{-C}$ was appraised by means of cycling experiments. During each run, the catalyst was separated through filtration followed by washing with ultrapure water and drying at 60 °C, which was then subjected to the next run of BPA degradation. The PDS concentration during the reaction was determined according to the previous work [37]. Electron paramagnetic resonance (EPR) spectra of ${}^{\bullet}\text{OH}/\text{SO}_4^{\bullet-}$ and ${}^1\text{O}_2$ in reaction systems were discerned on a Bruker A300 spectrometer with DMPO and 2,2,6,6-tetramethylpiperidine (TMP), respectively. The main degradation intermediates were identified with a Shimadzu GCMS-QP2020 NX gas chromatography-mass spectrometer. Specifically, the solid catalyst and reaction solution were harvested after filtration and then subjected to evaporation with a vacuum freeze-drying oven. Thereafter, 2 mL of dichloromethane and trimethylsilylated with 0.2 mL of N,O-bis(trimethylsilyl)trifluoroacetamide (BTFA, TCI) were added in sequence to dissolve and silanize the solid residues at 60 °C for 30 min. The precipitate was then separated through centrifugation prior to the chromatographic analysis. The chromatographic conditions were as follows: the initial column temperature was maintained at 30 °C for 2 min followed by ramping to 280 °C with a heating rate of 6 °C min⁻¹.

2.5. Theoretical calculation

The spin polarized electronic structures of all models were computed with density function theory (DFT) using projected augmented wave (PAW), which was implemented in Vienna Ab initio Simulation Package (VASP) code [38]. The exchange-correlation interactions were treated with the generalized gradient approximation (GGA) parameterized by Perdew-Burke-Ernzerhof (PBE) functions [39]. The cutoff energy of plane-wave basis and the convergence criterion for geometry optimization were set to be 400 eV and 0.02 eV Å⁻¹, respectively. The adsorption energy was defined by.

$$E_{\text{ads}} = E_{(\text{surf} + \text{mol})} - E_{(\text{surf})} - E_{(\text{mol})} \quad (1)$$

where $E_{(\text{surf} + \text{mol})}$ is the total energy of a surface interacting with a molecule, and $E_{(\text{surf})}$ and $E_{(\text{mol})}$ are energies for the clean surface and free molecule, respectively.

3. Results and discussion

3.1. Characterization of catalysts

The sodium citrate was carbonized to engage as oxygen-containing carbon support (marked as CS) to immobilize Co species, where the physicochemical property of CS could be visualized from our previous work [26]. The X-ray diffraction (XRD) pattern of $\text{Co}_{\text{SA}}\text{-N}_3\text{-C}$ shows the similar diffraction mode with that of nitrogen-doped carbon support (N-C) (Fig. S1), in which two broad peaks appear at around 24.7° and 44.1° corresponding to graphitic (002) and (100) planes [40,41], respectively. This suggests the carbonaceous nature of N-C and $\text{Co}_{\text{SA}}\text{-N}_3\text{-C}$, and meanwhile, no characteristic peak assigned to Co crystals is noted in $\text{Co}_{\text{SA}}\text{-N}_3\text{-C}$. Conversely, a set of peaks referring to crystallized Co species emerge in the Co nanoparticles supported on nitrogen-doped carbon (Co-N-C), reflecting that glucose exerts a vital function in the isolation and atomic dispersion of Co atoms on the CS [26,42]. The X-ray photoelectron spectroscopy (XPS) measurement (Table S1) reveals the nitrogen component in as-prepared samples after nitrogen doping, which is validated by the emergence of C—N peak in the XPS C 1s spectra (Fig. S2). The N-C and Co-N-C present the lamellar nanostructures, as visualized by scanning electron microscopy (SEM) images (Fig. S3a, c), which are consistent with that of CS from our previous work [26]. The transmission electron microscopy (TEM) images (Fig. S3b, d) confirm the laminar architecture of N-C and Co-N-C, while the Co nanoparticles can be obviously noticeable in Co-N-C,

consistent with the above XRD analysis. The SEM image (Fig. S4a) presents that $\text{Co}_{\text{SA}}\text{-N}_3\text{-C}$ resembles the sheet-like and porous nanostructure of N-C. The TME image (Fig. S4b) and high-resolution TEM (HRTEM) image of randomly selected areas (Fig. S4c) verify the absence of crystalline Co species in the lamellar architecture of $\text{Co}_{\text{SA}}\text{-N}_3\text{-C}$. The selected area electron diffraction (SAED) (Fig. S4d) reveals a ring-like pattern, illustrating the poor crystallinity of $\text{Co}_{\text{SA}}\text{-N}_3\text{-C}$, which coincides well with the XRD measurement. High-angle annular dark-field scanning transmission electron microscopy (HAADF-STEM) image (Fig. 1a) further validates the laminar structure of $\text{Co}_{\text{SA}}\text{-N}_3\text{-C}$ without the formation of metallic Co crystals. The representative elemental mapping images (Fig. 1b) illuminate that N and Co atoms are distributed uniformly over the entire carbon skeleton of $\text{Co}_{\text{SA}}\text{-N}_3\text{-C}$. Moreover, numerous luminous dots (highlighted by red dotted circles) can be readily discerned in the magnified HAADF-STEM image (Fig. 1c), substantiating the atomic dispersion of Co atoms in $\text{Co}_{\text{SA}}\text{-N}_3\text{-C}$. The loading amount of Co species in the $\text{Co}_{\text{SA}}\text{-N}_3\text{-C}$ sample was detected to be 0.25 at % and 1.20 wt% by XPS and inductively coupled plasma optical emission spectrometry (ICP-OES) (Table S1), respectively. The N_2 adsorption-desorption isotherms of N-doped carbon-based materials (Fig. S5a-c) display the same type IV curves with their specific surface areas being summarized in Table S1. The corresponding pore size distribution curves (Fig. S5d) manifest the mesoporous structures of these N-doped carbon-based samples.

To explore the coordination environment of the single-atomic Co center in $\text{Co}_{\text{SA}}\text{-N}_3\text{-C}$, the synchrotron-based X-ray absorption fine structure (XAFS) spectroscopy was undertaken. As depicted in Co K-edge X-ray absorption near-edge structure (XANES) spectrum (Fig. 1d), the near-edge absorption energy of $\text{Co}_{\text{SA}}\text{-N}_3\text{-C}$ is located between CoO and Co_3O_4 references, implying the Co atom is in an oxidation state between Co^{2+} and Co^{3+} . The Co K-edge Fourier transforms (FT) extended X-ray absorption fine structure (EXAFS) spectrum (Fig. 1e) reveals a strong peak associated with the scattering of Co—N coordination [32], without the scattering peak derived from Co—Co bonding, which demonstrates the atomic dispersion of Co species over $\text{Co}_{\text{SA}}\text{-N}_3\text{-C}$. In addition, the coordination configuration of Co—N path in the first coordination shell was investigated by the quantitative EXAFS fitting. As depicted in Fig. 1f and S6, the EXAFS fitting results in R and k spaces match well with the experimental data. Specifically, the average coordination number of Co—N was acquired to be 3.0, and the corresponding average bond length was 1.94 Å (Table S2), which illustrates the construction of single-atomic Co—N₃ moiety in $\text{Co}_{\text{SA}}\text{-N}_3\text{-C}$. The HR-XPS N 1s spectrum of $\text{Co}_{\text{SA}}\text{-N}_3\text{-C}$ can be fitting into five typical peaks corresponding to pyridinic N, Co—N [43], pyrrolic N, graphitic N, and oxidized N (Fig. 1g), in which the appearance of the Co—N peak also attests to the coordination of Co with N atoms. Compared to N-C, the pyridinic N peak shifts toward lower binding energy with the decoration of the Co atom in that of $\text{Co}_{\text{SA}}\text{-N}_3\text{-C}$ (Fig. 1g), suggesting that pyridinic N is inclined to immobilize the Co atom in the form of coordination bond. In the geometrical configuration, the coordination of a Co atom with three N atoms could constitute the Co—N₃ structure with and without the formation of carbon vacancy, of which the correspondingly optimized atomic structures of Co-N₃-C_V and Co-N₃-C are depicted in Fig. 1h. Density functional theory (DFT) calculations unraveled the formation energy for the Co-N₃-C model was lower than that for the Co-N₃-C_V structure, manifesting the more favorable construction of Co-N₃-C configuration without the formation of carbon defect. The analogical Raman spectra of N-C and $\text{Co}_{\text{SA}}\text{-N}_3\text{-C}$ (Fig. S7) reflects that the atomic dispersion of Co atoms does not undermine the fundamental structure of carbon skeleton in $\text{Co}_{\text{SA}}\text{-N}_3\text{-C}$. The above analysis results corroborate the successful synthesis of the $\text{Co}_{\text{SA}}\text{-N}_3\text{-C}$ catalyst with the construction of single-atomic Co—N₃ sites.

3.2. Persulfate activation performance

The persulfate activation performance was appraised through

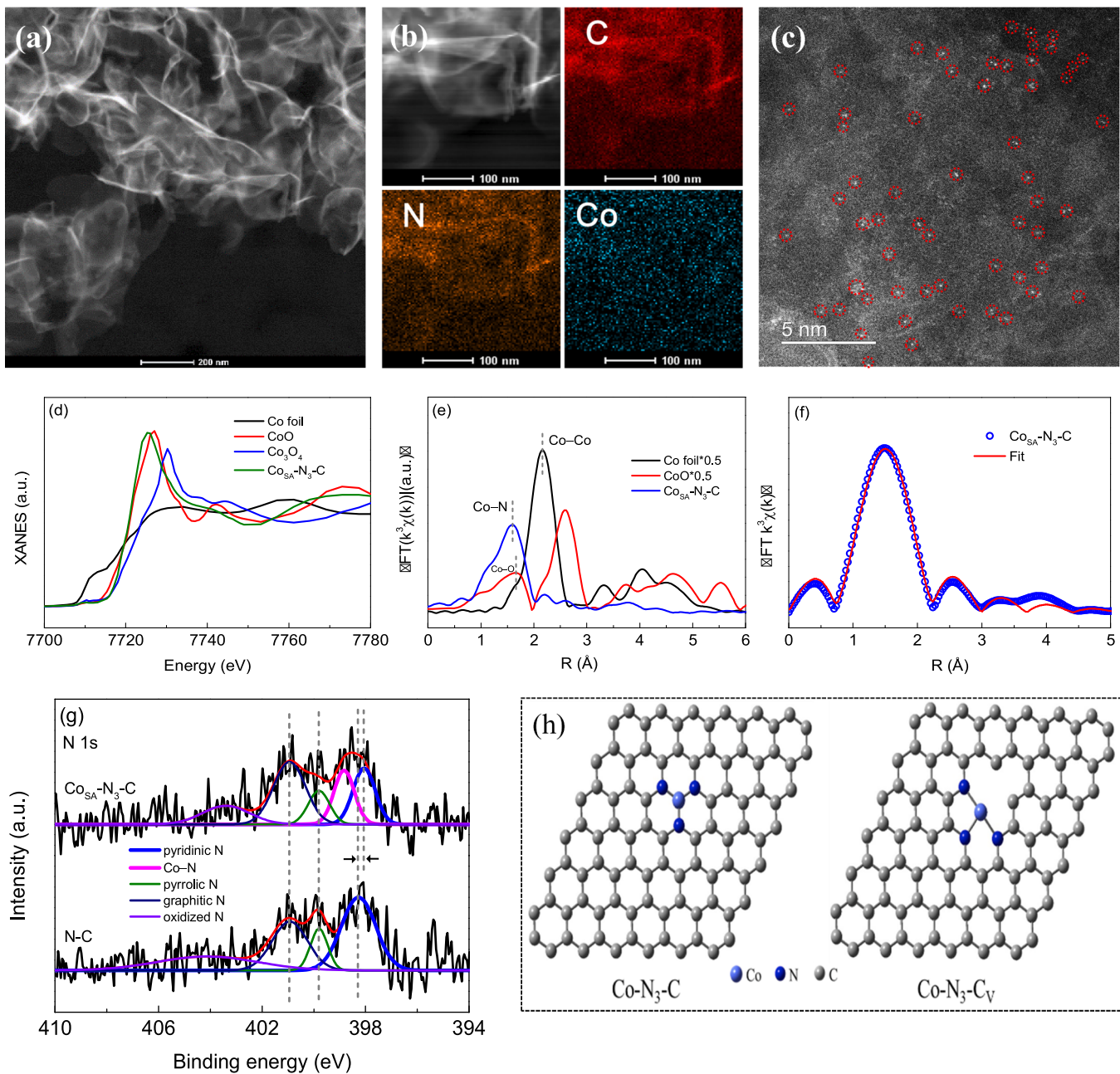


Fig. 1. (a) HAADF-STEM image and (b) EDX element mapping images of $\text{Co}_{\text{SA}}\text{-N}_3\text{-C}$. (c) Magnified HAADF-STEM image of $\text{Co}_{\text{SA}}\text{-N}_3\text{-C}$. (d) Normalized Co K-edge XANES and (e) FT-EXAFS spectra of $\text{Co}_{\text{SA}}\text{-N}_3\text{-C}$ and reference samples. (f) EXAFS fitting curve of $\text{Co}_{\text{SA}}\text{-N}_3\text{-C}$ at R space. (g) HR-XPS spectra of N 1s for N-C and $\text{Co}_{\text{SA}}\text{-N}_3\text{-C}$. (h) Optimized atomic structures of $\text{Co}\text{-N}_3\text{-C}$ and $\text{Co}\text{-N}_3\text{-C}_V$, including C (gray), N (blue), and Co (purple) atoms. (For interpretation of the references to colour in this figure legend, the reader is referred to the web version of this article.)

bisphenol A (BPA, a representative refractory organic contaminant) elimination over $\text{Co}_{\text{SA}}\text{-N}_3\text{-C}$ in the presence of PDS. As shown in Fig. 2a, individual PDS or CS causes inappreciable removal of BPA ruling out the oxidative ability of PDS and adsorption of CS in BPA elimination. The couple of CS and PDS brings about insignificant BPA removal, suggesting the rather limited reactivity of CS in activating PDS. In the absence of PDS, the $\text{Co}_{\text{SA}}\text{-N}_3\text{-C}$ alone produces approximately 30% BPA removal efficiency, which can be attributable to the adsorptive capacity of the catalyst. However, the combination of $\text{Co}_{\text{SA}}\text{-N}_3\text{-C}$ and PDS gives rise to highly efficient BPA abatement with complete oxidation of BPA within 4 min, indicating the prominent catalytic activity of $\text{Co}_{\text{SA}}\text{-N}_3\text{-C}$ in PDS activation. The assessment of effects of catalyst dosage and PDS concentration on BPA degradation (Fig. S8a, b) suggests the existence of optimum dosages of $\text{Co}_{\text{SA}}\text{-N}_3\text{-C}$ and PDS to be 0.05 g L^{-1} and 2 mM ,

respectively. To underline the catalytic performance of $\text{Co}_{\text{SA}}\text{-N}_3\text{-C}$, the PDS activation performance on $\text{Co}\text{-N-C}$ and the single-atom Co catalyst with the coordination number of four ($\text{Co}_{\text{SA}}\text{-N}_4\text{-C}$) was evaluated and also compared. Of note is that the $\text{Co}_{\text{SA}}\text{-N}_4\text{-C}$ was synthesized in parallel to that of $\text{Co}_{\text{SA}}\text{-N}_3\text{-C}$ except for the decrease of pyrolysis temperature from 900°C to 800°C . The higher N amount of $\text{Co}_{\text{SA}}\text{-N}_4\text{-C}$ than that of $\text{Co}_{\text{SA}}\text{-N}_3\text{-C}$ can be evidenced by XPS analysis results (Table S1) and the stronger Co—N peak intensity in FT-EXAFS spectrum of $\text{Co}_{\text{SA}}\text{-N}_4\text{-C}$ (Fig. S9a). The XRD pattern (Fig. S9b) and FT-EXAFS spectrum (Fig. S9a) along with EXAFS fitting (Fig. S9c, d, Table S2) validate the atomically dispersed Co sites with one Co atom coordinated by four N atoms for the formation of $\text{Co}\text{-N}_4$ structure in $\text{Co}_{\text{SA}}\text{-N}_4\text{-C}$. Moreover, these three samples of $\text{Co}\text{-N-C}$, $\text{Co}_{\text{SA}}\text{-N}_3\text{-C}$ and $\text{Co}_{\text{SA}}\text{-N}_4\text{-C}$ possess comparable Co contents (Table S1). The limited BPA removal by $\text{Co}\text{-N-C}$ or $\text{Co}_{\text{SA}}\text{-N}_4\text{-C}$

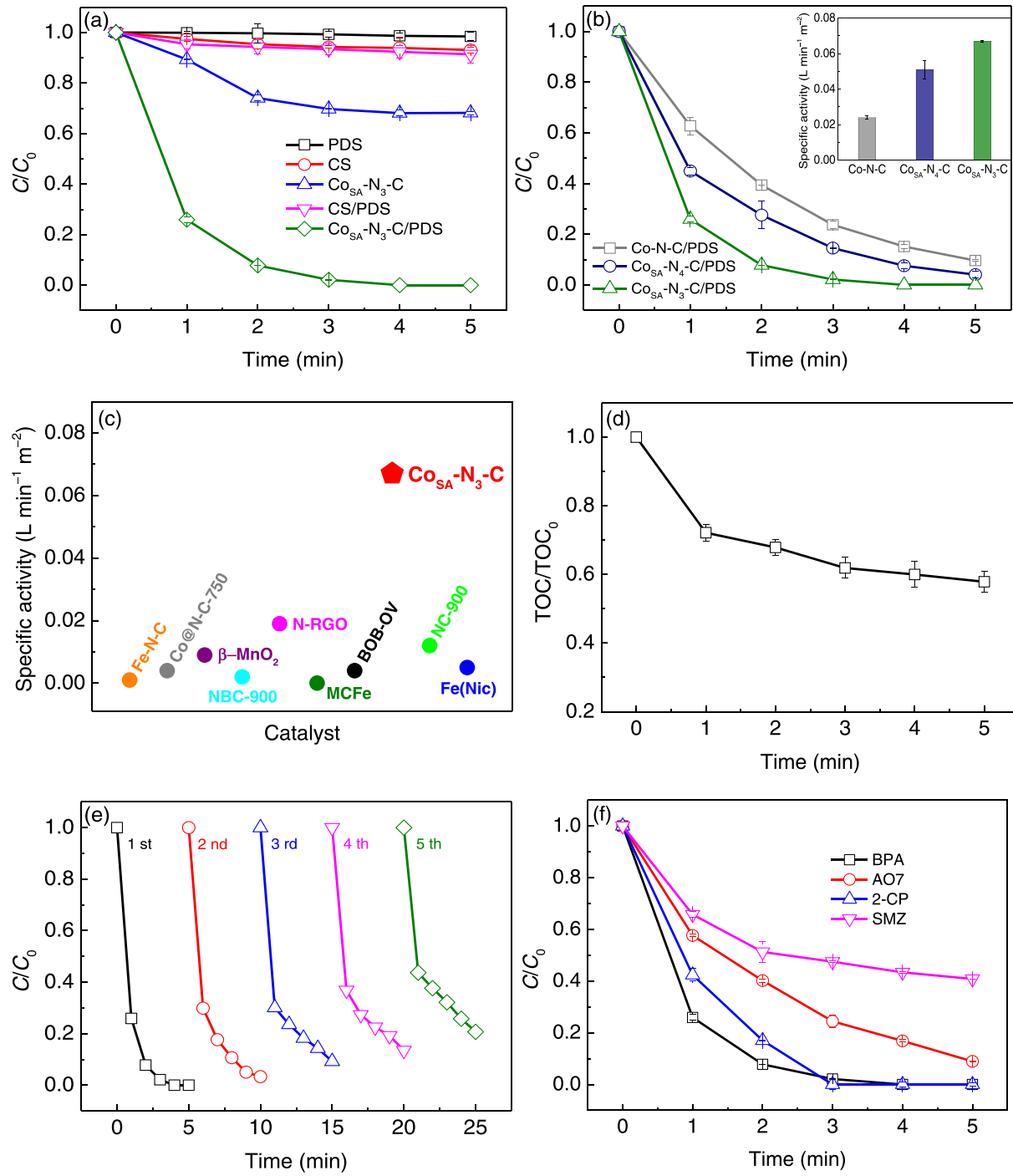


Fig. 2. (a) Removal of BPA in diverse systems. (b) PDS activation over Co-N-C, $\text{Co}_{\text{SA}}\text{-N}_4\text{-C}$ and $\text{Co}_{\text{SA}}\text{-N}_3\text{-C}$ (inset of specific activity comparison). (c) Specific activity comparison of $\text{Co}_{\text{SA}}\text{-N}_3\text{-C}$ with recently reported catalysts in PDS activation. (d) TOC removal in $\text{Co}_{\text{SA}}\text{-N}_3\text{-C}/\text{PDS}$. (e) Stability test of $\text{Co}_{\text{SA}}\text{-N}_3\text{-C}$. (f) Degradation of different pollutants in $\text{Co}_{\text{SA}}\text{-N}_3\text{-C}/\text{PDS}$. Reaction conditions: [organic pollutant] = 50 μM ; [catalyst] = 0.05 g L^{-1} ; [PDS] = 2 mM; [Temp] = 30 °C; initial pH = 6.4.

alone (Fig. S10) reflects the finite contribution of adsorption to the elimination of BPA. As depicted in Fig. 2b, the $\text{Co}_{\text{SA}}\text{-N}_3\text{-C}$ reaches the optimum catalytic activity in the activation of PDS, followed by the $\text{Co}_{\text{SA}}\text{-N}_4\text{-C}$ and Co-N-C. Normalizing the BPA oxidation rate constant to specific surface area and dosage of the catalyst reflects the optimal specific activity of $\text{Co}_{\text{SA}}\text{-N}_3\text{-C}$ [26,40], which follows the order of $\text{Co}_{\text{SA}}\text{-N}_3\text{-C}$ ($0.067 \text{ L min}^{-1} \text{ m}^{-2}$) > $\text{Co}_{\text{SA}}\text{-N}_4\text{-C}$ ($0.051 \text{ L min}^{-1} \text{ m}^{-2}$) > Co-N-C ($0.024 \text{ L min}^{-1} \text{ m}^{-2}$) (inset of Fig. 2b) based on the reaction rate constants acquired from the pseudo-first-order kinetics ($\ln(C/C_0) = -kt$, where C is the BPA concentration at a certain reaction time (t),

and C_0 is the initial BPA concentration, k is the reaction rate constant) (Fig. S11) and specific surface areas (Fig. S12, Table S1). This demonstrates that (i) single-atom metal catalysts outperform the metal nanoparticles supported catalyst in PDS activation and (ii) lowering coordination number can enhance PDS conversion over single-atom Co catalysts. Moreover, the specific activity comparison of $\text{Co}_{\text{SA}}\text{-N}_3\text{-C}$ with the currently reported state-of-the-art catalysts was conducted to highlight the admirable catalytic activity of $\text{Co}_{\text{SA}}\text{-N}_3\text{-C}$ in PDS activation (see Table S3 for more details). As displayed in Fig. 2c, the specific activity of $\text{Co}_{\text{SA}}\text{-N}_3\text{-C}$ is apparently higher than that of existing catalysts, signifying

the superior catalytic performance of $\text{Co}_{\text{SA}}\text{-N}_3\text{-C}$ for PDS conversion.

In addition, the decrease of total organic carbon (TOC) (Fig. 2d) suggests the effective BPA degradation over $\text{Co}_{\text{SA}}\text{-N}_3\text{-C}$ in the presence of PDS. Meanwhile, the stability of the catalyst was evaluated through cycling experiments. The $\text{Co}_{\text{SA}}\text{-N}_3\text{-C}$ maintains approximately 80% of its original catalytic performance after the fifth cycle (Fig. 2e), indicating the favorable durability of $\text{Co}_{\text{SA}}\text{-N}_3\text{-C}$. The inappreciable change in the XRD pattern of $\text{Co}_{\text{SA}}\text{-N}_3\text{-C}$ after PDS activation (Fig. S13a) excludes metal aggregation during catalytic reaction, and slight leaching of Co ion (0.03 mg L^{-1} , measured by ICP-OES) was detected, with its insignificant role in PDS activation (Fig. S13b). Meanwhile, the atomically dispersed Co atoms can be also observed on the used $\text{Co}_{\text{SA}}\text{-N}_3\text{-C}$ (Fig. S13c). In particular, the adsorption effect of the used $\text{Co}_{\text{SA}}\text{-N}_3\text{-C}$ hardly causes the decrease of BPA removal (Fig. S14), while the decrease in the catalytic activity of $\text{Co}_{\text{SA}}\text{-N}_3\text{-C}$ can be mainly ascribed to (i) the slight loss of the active Co species due to the metal leaching (Table S1) and (ii) the adsorption of partial intermediates of BPA degradation on the surface of $\text{Co}_{\text{SA}}\text{-N}_3\text{-C}$ during recycle (Figs. S15, S16; Table S4), which is consistent with our previous work [26]. In addition to BPA, the efficient oxidation of other recalcitrant organics such as acid orange 7 (AO7, an organic dye), 2-chlorophenol (2-CP, a pesticide precursor) and sulfamethoxazole (SMZ, an antibiotic) (Fig. 2f) reflects the effectiveness of $\text{Co}_{\text{SA}}\text{-N}_3\text{-C}$ for catalyzing the degradation of a broad spectrum of organic contaminants via PDS activation by elucidating the limited contribution of adsorption to the removal of such organic pollutants on $\text{Co}_{\text{SA}}\text{-N}_3\text{-C}$ (Fig. S17).

3.3. Mechanistic insights into PDS conversion over $\text{Co}_{\text{SA}}\text{-N}_x\text{-C}$

Reactive oxygen species (ROS) are commonly produced upon PDS activation [44]. In the case of PDS conversion by $\text{Co}_{\text{SA}}\text{-N}_3\text{-C}$, the ROS formation was explored through electron paramagnetic resonance (EPR) measurements and inhibition tests. As shown in Fig. 3a, besides the signal from oxidized 5,5-dimethyl-1-pyrroline N-oxide (DMPO) [45], characteristic peaks of DMPO-OH and DMPO- $\text{SO}_4^{\cdot-}$ appear evidently in the $\text{Co}_{\text{SA}}\text{-N}_3\text{-C}/\text{PDS}$ system by using DMPO as a trapping reagent, illustrating the production of $\cdot\text{OH}$ and $\text{SO}_4^{\cdot-}$ [46]. The signal intensity of $\cdot\text{OH}$ is stronger than that of $\text{SO}_4^{\cdot-}$, which can be attributable to rapid transformation of $\text{DMPO-SO}_4^{\cdot-}$ to DMPO-OH via nucleophilic substitution reaction [44,47,48]. In addition to radicals, the yield of nonradical species such as ${}^1\text{O}_2$ was also explored. When 2,2,6,6-tetramethyl-4-piperidinol (TMP) was presented, the couple of $\text{Co}_{\text{SA}}\text{-N}_3\text{-C}$ and PDS produces no representative TMP- ${}^1\text{O}_2$ signal (Fig. 3b), which rules out the production of ${}^1\text{O}_2$ during PDS conversion by $\text{Co}_{\text{SA}}\text{-N}_3\text{-C}$. The quenching test results match well with the EPR analysis. As shown in Fig. 3c, the addition of *tert*-butyl alcohol (TBA, a $\cdot\text{OH}$ quencher) inhibits the degradation of BPA, and the inhibition effect increases with the augment of TBA concentration. The similar phenomenon is noted for ethanol (EtOH, a scavenger for both $\cdot\text{OH}$ and $\text{SO}_4^{\cdot-}$), while the suppression effect of EtOH on BPA oxidation is more significant relative to that of TBA. In contrast, the oxidation of BPA is hardly suppressed with furfuryl alcohol (FFA, a ${}^1\text{O}_2$ quencher). This illustrates the primary role of $\text{SO}_4^{\cdot-}$ in oxidative degradation of BPA by $\text{Co}_{\text{SA}}\text{-N}_3\text{-C}$ with PDS. In the

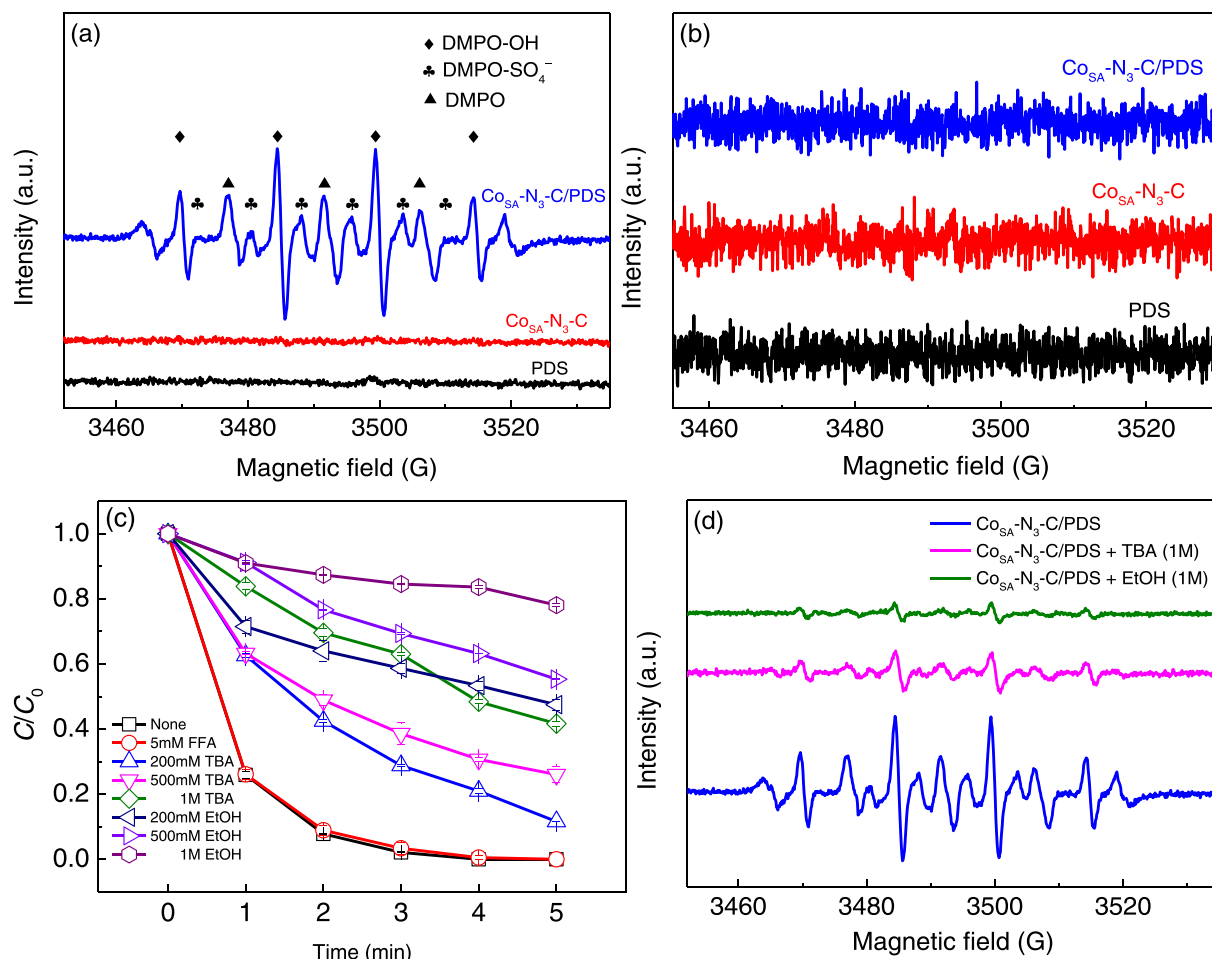


Fig. 3. EPR spectra for (a) $\cdot\text{OH}/\text{SO}_4^{\cdot-}$ in the presence of DMPO and (b) ${}^1\text{O}_2$ in the presence of TMP in various systems. (c) Effect of scavengers on BPA oxidation over $\text{Co}_{\text{SA}}\text{-N}_3\text{-C}$ via PDS activation. (d) EPR spectra of $\cdot\text{OH}/\text{SO}_4^{\cdot-}$ for $\text{Co}_{\text{SA}}\text{-N}_3\text{-C}/\text{PDS}$ with TBA and EtOH. Reaction conditions: $[\text{BPA}] = 50 \mu\text{M}$; $[\text{catalyst}] = 0.05 \text{ g L}^{-1}$; $[\text{PDS}] = 2 \text{ mM}$; $[\text{Temp}] = 30^\circ\text{C}$; initial pH = 6.4.

meanwhile, the EPR signals of DMPO-OH and DMPO-SO₄⁻ reduce pronouncedly upon the addition of TBA and EtOH into the suspension of Co_{SA}-N₃-C and PDS, while the presence of EtOH brings about a more significant decrease in the intensities of •OH and SO₄²⁻ signals (Fig. 3d), in line with the above quenching test results. This further confirms that •OH and SO₄²⁻ are generated during PDS activation by Co_{SA}-N₃-C, and SO₄²⁻ is mainly responsible for catalytic oxidation of BPA.

To identify the active centers in Co_{SA}-N₃-C for PDS conversion into •OH and SO₄²⁻, the PDS activation over N-doped carbon (N-C) and Co_{SA}-N₃-C was undertaken. As compared to N-C, a dramatic enhancement of PDS activation is noticeable for Co_{SA}-N₃-C (Fig. 4a), suggesting the crucial role of single Co atom in the decomposition of PDS. Moreover, the influence of 1,10-phenanthroline (Phen) on the activation of PDS over Co_{SA}-N₃-C was investigated, since 1,10-phenanthroline can effectively chelate with Co atoms but hardly adsorb on carbon-based materials. As depicted in Fig. 4b, the addition of 1,10-phenanthroline

into the Co_{SA}-N₃-C/PDS system drastically suppresses BPA degradation, validating that the single-atomic Co sites in Co_{SA}-N₃-C are the active centers for PDS accessibility and successive conversion. In addition, the XAFS measurement of Co_{SA}-N₃-C after PDS activation was performed to explore the mutual interaction of Co_{SA}-N₃-C with PDS. The XANES spectra in Fig. 4c illustrate slight positive energy shift in the absorption edge of the Co K-edge for Co_{SA}-N₃-C after PDS activation, which manifests the increase of oxidation state of the Co atom in the course of PDS conversion process [26,49]. This means the occurrence of electron transfer from the single Co atom toward the PDS molecule leading to PDS reduction over the single-atomic Co sites for •OH and SO₄²⁻ production. Meanwhile, the major absorption peak for the Co K-edge undergoes an evident increase in the intensity for Co_{SA}-N₃-C after the activation of PDS, demonstrating the strong interaction between single-atom Co active sites and PDS. The electrochemical impedance spectroscopy (EIS) spectra (Fig. S18a) further verifies the higher

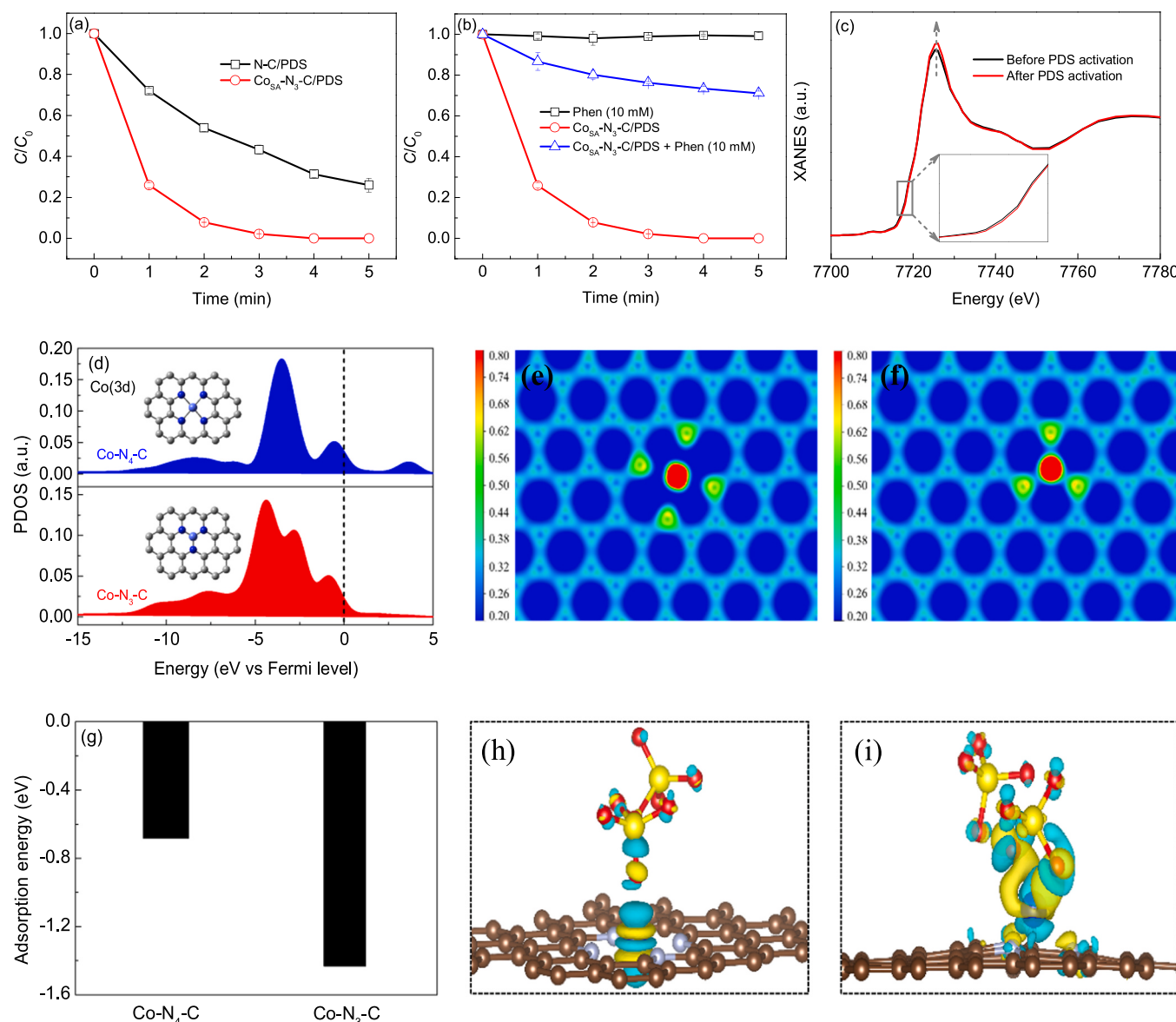


Fig. 4. (a) PDS activation by N-C and Co_{SA}-N₃-C. (b) Effect of 1,10-phenanthroline (Phen) on BPA degradation over Co_{SA}-N₃-C with PDS. (c) Normalized Co K-edge XANES spectra of Co_{SA}-N₃-C before and after PDS activation. (d) The d-states of Co atom in optimized Co-N₄-C and Co-N₃-C structures. Two-dimensional electron density distribution images of (e) Co-N₄-C and (f) Co-N₃-C models. (g) Adsorption energy of PDS on Co-N₄-C and Co-N₃-C models. The difference of electron density for PDS adsorbed on (h) Co-N₄-C and (i) Co-N₃-C models. Yellow and cyan regions represent electron accumulation and electron depletion, respectively. Reaction conditions: [BPA] = 50 μM; [catalyst] = 0.05 g L⁻¹; [PDS] = 2 mM; [Temp] = 30 °C; initial pH = 6.4. (For interpretation of the references to colour in this figure legend, the reader is referred to the web version of this article.)

electron mobility of $\text{Co}_{\text{SA}}\text{-N}_3\text{-C}$ than that of $\text{Co}_{\text{SA}}\text{-N}_4\text{-C}$ due to the smaller arc radius in $\text{Co}_{\text{SA}}\text{-N}_3\text{-C}$, which is more favorable to electron transfer between $\text{Co}_{\text{SA}}\text{-N}_3\text{-C}$ and PDS. After the addition of PDS, the arc radius of the $\text{Co}_{\text{SA}}\text{-N}_3\text{-C}$ electrode decrease more significantly relative to that of the $\text{Co}_{\text{SA}}\text{-N}_4\text{-C}$ electrode (Fig. S18b, c), which reflects the occurrence of stronger electron transport of $\text{Co}_{\text{SA}}\text{-N}_3\text{-C}$ with PDS. Density functional theory (DFT) calculations were further conducted to furnish theoretical insights into the interaction of $\text{Co}_{\text{SA}}\text{-N}_x\text{-C}$ catalysts with PDS and the difference of $\text{Co}_{\text{SA}}\text{-N}_3\text{-C}$ and $\text{Co}_{\text{SA}}\text{-N}_4\text{-C}$ in PDS conversion performance. As displayed in Fig. 4d, the d-orbital partial density of states (PDOS) of Co atoms in $\text{Co}_{\text{SA}}\text{-N}_3\text{-C}$ near the Fermi level is higher in comparison with that of $\text{Co}_{\text{SA}}\text{-N}_4\text{-C}$, implying that the $\text{Co}_{\text{SA}}\text{-N}_3\text{-C}$ delivers a stronger interaction with PDS relative to $\text{Co}_{\text{SA}}\text{-N}_4\text{-C}$ [50,51]. The two-dimensional electron density distribution images (Fig. 4e, f) demonstrate the highest electron density of Co atom in both $\text{Co}_{\text{SA}}\text{-N}_4\text{-C}$ and $\text{Co}_{\text{SA}}\text{-N}_3\text{-C}$, whereas the Co atom in $\text{Co}_{\text{SA}}\text{-N}_3\text{-C}$ possesses much greater electron density as compared to that in $\text{Co}_{\text{SA}}\text{-N}_4\text{-C}$, which can facilitate PDS attachment onto the single-atomic Co site in $\text{Co}_{\text{SA}}\text{-N}_3\text{-C}$. The much larger adsorption energy of PDS on $\text{Co}\text{-N}_3\text{-C}$ than that on $\text{Co}\text{-N}_4\text{-C}$ (Fig. 4g) corroborates the higher affinity of the single Co atom in $\text{Co}_{\text{SA}}\text{-N}_3\text{-C}$ to the PDS molecule. The similar trend is also noted for the elongation of O—O bond length after PDS adsorption. Specifically, the O—O bond length is elongated from 1.491 Å in free PDS to 1.505 and 1.519 Å after PDS accessibility on single Co atoms in $\text{Co}\text{-N}_4\text{-C}$ and $\text{Co}\text{-N}_3\text{-C}$ models, respectively. The elongation of O—O bond length upon PDS adsorption onto the single atomic Co sites suggests the efficient PDS activation over $\text{Co}_{\text{SA}}\text{-N}_4\text{-C}$ and $\text{Co}_{\text{SA}}\text{-N}_3\text{-C}$ catalysts. However, the stretching of O—O bond is more significant when PDS was attached on the single Co atom in the $\text{Co}\text{-N}_3\text{-C}$ model, which implies the more efficient PDS conversion over the single atomic Co site of $\text{Co}_{\text{SA}}\text{-N}_3\text{-C}$. Moreover, the difference in electron density for $\text{Co}_{\text{SA}}\text{-N}_4\text{-C}$ and $\text{Co}_{\text{SA}}\text{-N}_3\text{-C}$ after PDS adsorption was also calculated to visualize the incorporation between PDS and $\text{Co}_{\text{SA}}\text{-N}_x\text{-C}$ catalysts. As shown in Fig. 4h, i, the electron exchange of the single-atomic Co sites in $\text{Co}_{\text{SA}}\text{-N}_x\text{-C}$ with PDS indeed takes place, and more electrons tend to be transferred from the single Co atom toward PDS after lowering coordination number of four in $\text{Co}_{\text{SA}}\text{-N}_4\text{-C}$ to three in $\text{Co}_{\text{SA}}\text{-N}_3\text{-C}$. The Bader charge analysis further confirmed much more electron transport from the single-atomic Co site in $\text{Co}_{\text{SA}}\text{-N}_3\text{-C}$ toward the PDS molecule (0.102 e) than that in $\text{Co}_{\text{SA}}\text{-N}_4\text{-C}$ (0.042 e), which is more conducive to PDS reduction over $\text{Co}_{\text{SA}}\text{-N}_3\text{-C}$, in line with the above EIS analysis results.

In addition to theoretical computations, the decomposition of PDS and generation of radicals on $\text{Co}_{\text{SA}}\text{-N}_4\text{-C}$ and $\text{Co}_{\text{SA}}\text{-N}_3\text{-C}$ were explored and compared. As can be observed from Fig. 5a, a higher PDS decomposition efficiency is noted for $\text{Co}_{\text{SA}}\text{-N}_3\text{-C}$ compared with $\text{Co}_{\text{SA}}\text{-N}_4\text{-C}$. In the meantime, the paramagnetic $\cdot\text{OH}$ and $\text{SO}_4^{\bullet-}$ signal intensities in $\text{Co}_{\text{SA}}\text{-N}_3\text{-C}/\text{PDS}$ are stronger than those in $\text{Co}_{\text{SA}}\text{-N}_4\text{-C}/\text{PDS}$ (Fig. 5b), indicating the production of a larger amount of $\cdot\text{OH}$ and $\text{SO}_4^{\bullet-}$ over $\text{Co}_{\text{SA}}\text{-N}_3\text{-C}$ relative to $\text{Co}_{\text{SA}}\text{-N}_4\text{-C}$ via PDS activation. These experimental results are consistent with the above DFT calculations that lowering coordination number on $\text{Co}_{\text{SA}}\text{-N}_x\text{-C}$ catalysts can enhance the electron density of single Co atom, facilitating PDS adsorption and successive conversion into active radicals over the single-atomic Co site in $\text{Co}_{\text{SA}}\text{-N}_3\text{-C}$.

3.4. BPA degradation pathway and actual wastewater treatment application

In the $\text{Co}_{\text{SA}}\text{-N}_3\text{-C}/\text{PDS}$ system, the generated $\cdot\text{OH}$ and $\text{SO}_4^{\bullet-}$ can attack and oxidize the organic pollutant to produce intermediate products, which were identified through the gas chromatography-mass spectrometer (GC-MS) technique. The main intermediates are ascertained during BPA degradation by $\text{Co}_{\text{SA}}\text{-N}_3\text{-C}$ with PDS (Fig. 5c), and the relevant details and MS spectra are displayed in Table S4 and Fig. S16. According to the acquired results, a possible degradation pathway for BPA is proposed in Fig. 5d. More specifically, the BPA molecule firstly

underwent breakage to form p-tert-butyl phenol under oxidation of radicals, which was subsequently oxidized into 2,6-dihydroxybenzoic acid. After further attacking by radicals, the aromatic compound experienced ring-openness to yield pentaerythrol. Furthermore, pentaerythrol was transformed to glycerol, oxalic acid, and ethylene glycol, which were ultimately mineralized to CO_2 and H_2O . In addition, the applicability of $\text{Co}_{\text{SA}}\text{-N}_3\text{-C}$ was evaluated via BPA degradation in more complicated water matrix and the treatment of actual dyeing wastewater, which was harvested from the effluent after biological treatment in an Industrial Garden in Guangdong Province, China. As shown in Fig. 5e, although the existence of common environmental matrix such as NO_3^- , Cl^- and HCO_3^- , and humic acid (HA) retards the organic pollutant degradation kinetics, the efficient BPA oxidation over $\text{Co}_{\text{SA}}\text{-N}_3\text{-C}$ with PDS can be still fulfilled in such common water matrix after 5-min catalytic reactions. Moreover, after dissolving BPA into the actual dyeing wastewater, the efficient BPA elimination can be accomplished by $\text{Co}_{\text{SA}}\text{-N}_3\text{-C}$ via PDS activation (Fig. 5f). Furthermore, the effective treatment of actual dyeing wastewater can be also achieved by $\text{Co}_{\text{SA}}\text{-N}_3\text{-C}/\text{PDS}$. Specifically, four main peaks with high fluorescence intensities can be discerned in the three-dimensional excitation and emission matrix (3D-EEM) fluorescence spectrum (Fig. 5g), which refer to fulvic-like compounds (peaks A and B) and humic-like substances (peaks C and D) [48, 52]. After catalytic reaction by $\text{Co}_{\text{SA}}\text{-N}_3\text{-C}$ with PDS, the intensities of peaks A, B and C decrease significantly, and peak D even vanishes completely (Fig. 5h, i), which signifies the efficient abatement of organic compounds in the actual dyeing wastewater sample. The above results distinctly validate the remarkable reactivity of $\text{Co}_{\text{SA}}\text{-N}_3\text{-C}$ for PDS conversion and the prominent potential of $\text{Co}_{\text{SA}}\text{-N}_3\text{-C}$ in practical environmental cleanup mediated by persulfate.

4. Conclusions

We have developed a cascade anchoring strategy to synthesize the atomically dispersed Co—N_x sites with disparate coordination numbers by controlling the pyrolysis temperature. Remarkably, the optimal $\text{Co}_{\text{SA}}\text{-N}_3\text{-C}$ catalyst, with each isolated Co atom coordinated by three N atoms, displays excellent catalytic performance in PDS conversion with high specific activity of $0.067 \text{ L min}^{-1} \text{ m}^{-2}$, which is much superior to that of $\text{Co}_{\text{SA}}\text{-N}_4\text{-C}$ with single-atomic Co—N₄ sites and the most existing catalysts, rendering it one of the most active PDS activators. Theoretical calculations revealed that engineering the lower coordination number can increase the electron density of the single Co atom, which evidently enhances interaction between the single-atomic Co sites in $\text{Co}_{\text{SA}}\text{-N}_3\text{-C}$ with PDS and thus facilitates PDS conversion into active radicals, thereby boosting organic pollutant degradation. Moreover, the $\text{Co}_{\text{SA}}\text{-N}_3\text{-C}$ exhibits favorable stability in PDS activation and potential applicability in advanced oxidation of actual industrial wastewater. This work not only presents a rationally controlled approach to coordination number modulation of SACs but also offers a valuable route to design highly efficient metal-nitrogen-carbon catalysts for a variety of environmental applications.

CRediT authorship contribution statement

Xiaoying Liang: Data curation, Formal analysis, Methodology, Validation, Investigation, Visualization, Writing – original draft. **Di Wang:** Methodology, Software. **Zhiyu Zhao:** Validation, Investigation, Visualization. **Tong Li:** Validation. **Zhenhuan Chen:** Validation, Investigation, Visualization. **Yaowen Gao:** Conceptualization, Supervision, Writing – review & editing, Funding acquisition. **Chun Hu:** Supervision, Funding acquisition.

Declaration of Competing Interest

The authors declare that they have no known competing financial interests or personal relationships that could have appeared to influence

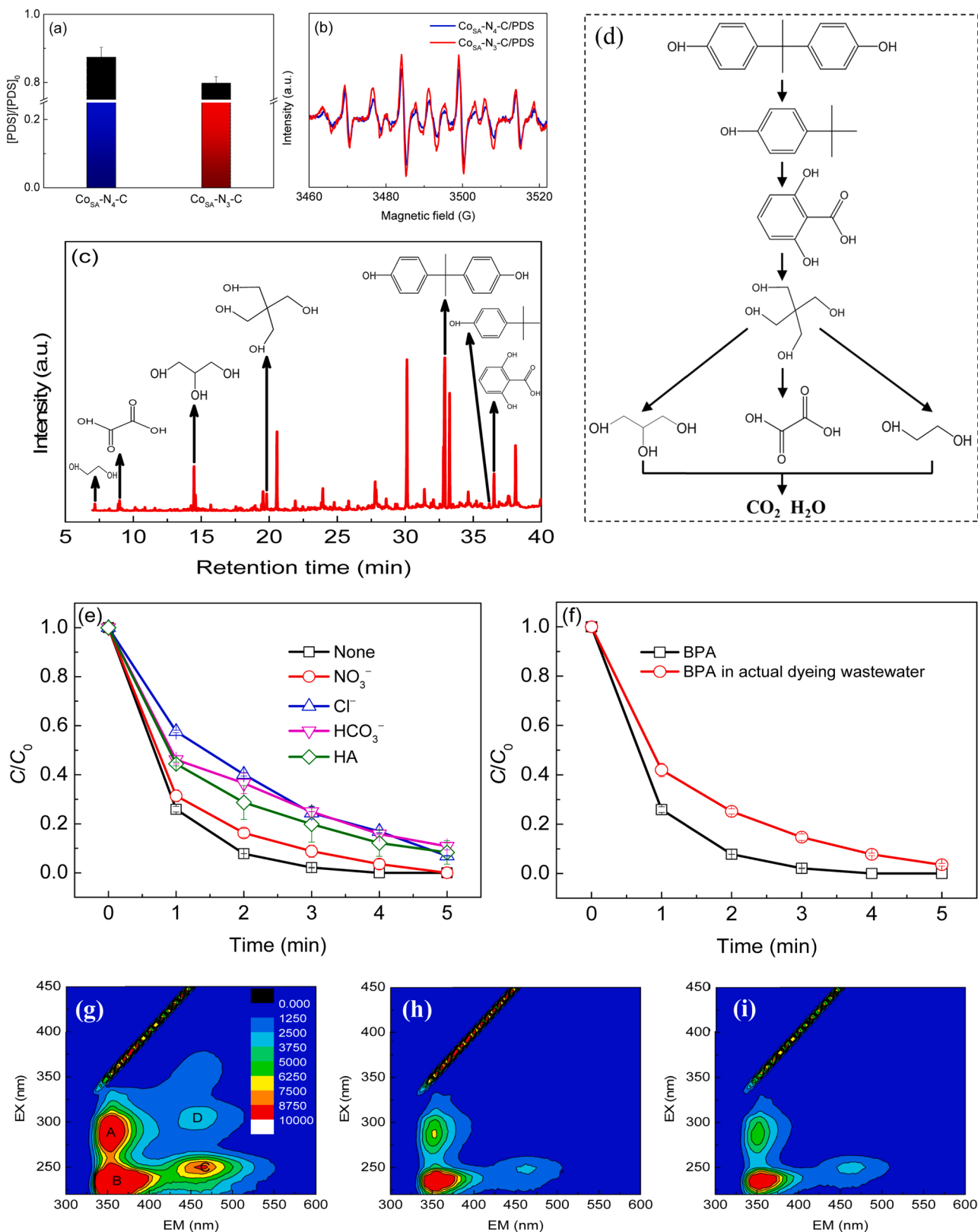


Fig. 5. (a) PDS decomposition over $\text{Co}_{\text{SA}}\text{-N}_4\text{-C}$ and $\text{Co}_{\text{SA}}\text{-N}_3\text{-C}$. (b) EPR spectra of $\cdot\text{OH}/\text{SO}_4^{\bullet-}$ over $\text{Co}_{\text{SA}}\text{-N}_4\text{-C}$ and $\text{Co}_{\text{SA}}\text{-N}_3\text{-C}$ via PDS activation. (c) GC-MS chromatogram for BPA degradation in $\text{Co}_{\text{SA}}\text{-N}_3\text{-C}/\text{PDS}$ after 2 min. (d) Possible BPA degradation pathway. (e) Effect of common inorganic anions and HA on BPA oxidation in $\text{Co}_{\text{SA}}\text{-N}_3\text{-C}/\text{PDS}$. (f) BPA degradation in actual dyeing wastewater sample. 3D-EEM fluorescence spectroscopy of the actual dyeing wastewater sample by $\text{Co}_{\text{SA}}\text{-N}_3\text{-C}/\text{PDS}$ after reaction for (g) 0 min, (h) 15 min and (i) 30 min. Reaction conditions: $[\text{BPA}] = 50 \mu\text{M}$; $[\text{catalyst}] = 0.05 \text{ g L}^{-1}$; $[\text{PDS}] = 2 \text{ mM}$; $[\text{NO}_3^-] = [\text{Cl}^-] = [\text{HCO}_3^-] = 2 \text{ mM}$; $[\text{HA}] = 2 \text{ mg L}^{-1}$; $[\text{Temp}] = 30^\circ\text{C}$. For GC-MS analysis, $[\text{BPA}] = 100 \mu\text{M}$.

the work reported in this paper.

Acknowledgements

This work was supported by the National Natural Science Foundation of China (51808142, 51838005), the introduced innovative R&D team project under the “The Pearl River Talent Recruitment Program” of Guangdong Province (2019ZT08L387), and Science and Technology Research Project of Guangzhou (202102020286). The authors are grateful to Shanghai Synchrotron Radiation Facility (SSRF) for the BL14W1 beamline.

Appendix A. Supporting information

Supplementary data associated with this article can be found in the online version at [doi:10.1016/j.apcatb.2021.120877](https://doi.org/10.1016/j.apcatb.2021.120877).

References

- [1] B.C. Hodges, E.L. Cates, J.H. Kim, Challenges and prospects of advanced oxidation water treatment processes using catalytic nanomaterials, *Nat. Nanotechnol.* 13 (2018) 642–650.
- [2] S. Waclawek, H.V. Lutze, K. Grüber, V.V.T. Padil, M. Černík, D.D. Dionysiou, Chemistry of persulfates in water and wastewater treatment: a review, *Chem. Eng. J.* 330 (2017) 44–62.
- [3] J. Wang, S. Wang, Activation of persulfate (PS) and peroxymonosulfate (PMS) and application for the degradation of emerging contaminants, *Chem. Eng. J.* 334 (2018) 1502–1517.
- [4] J. Lee, U.V. Gunten, J.H. Kim, Persulfate-based advanced oxidation: critical assessment of opportunities and roadblocks, *Environ. Sci. Technol.* 54 (2020) 3064–3081.
- [5] G.P. Anipsitakis, D.D. Dionysiou, Degradation of organic contaminants in water with sulfate radicals generated by the conjunction of peroxymonosulfate with cobalt, *Environ. Sci. Technol.* 37 (2003) 4790–4797.
- [6] G.P. Anipsitakis, D.D. Dionysiou, Radical generation by the interaction of transition metals with common oxidants, *Environ. Sci. Technol.* 38 (2004) 3705–3712.
- [7] E. Saputra, S. Muhammad, H. Sun, H.M. Ang, S. Wang, Different crystallographic one-dimensional MnO₂ nanomaterials and their superior performance in catalytic phenol degradation, *Environ. Sci. Technol.* 47 (2013) 5882–5887.
- [8] S. Zhu, X. Li, J. Kang, X. Duan, S. Wang, Persulfate activation on crystallographic manganese oxides: mechanism of singlet oxygen evolution for nonradical selective degradation of aqueous contaminants, *Environ. Sci. Technol.* 53 (2019) 307–315.
- [9] Z. Guo, C. Li, M. Gao, X. Han, Y. Zhang, W. Zhang, W. Li, Mn-O covalency governs the intrinsic activity of Co-Mn spinel oxides for boosted peroxymonosulfate activation, *Angew. Chem. Int. Ed.* 60 (2021) 274–280.
- [10] X. Zhou, A. Jawad, M. Luo, C. Luo, T. Zhang, H. Wang, J. Wang, S. Wang, Z. Chen, Z. Chen, Regulating activation pathway of Cu/persulfate through the incorporation of unreducible metal oxides: pivotal role of surface oxygen vacancies, *Appl. Catal. B Environ.* 286 (2021) 119914–119925.
- [11] C. Wang, S. Jia, Y. Zhang, Y. Nian, Y. Wang, Y. Han, Y. Liu, H. Ren, S. Wu, K. Yao, X. Han, Catalytic reactivity of Co₃O₄ with different facets in the hydrogen abstraction of phenol by persulfate, *Appl. Catal. B Environ.* 270 (2020) 118819–118830.
- [12] T. Zeng, X. Zhang, S. Wang, H. Niu, Y. Cai, Spatial confinement of a Co₃O₄ catalyst in hollow metal-organic frameworks as a nanoreactor for improved degradation of organic pollutants, *Environ. Sci. Technol.* 49 (2015) 2350–2357.
- [13] X. Li, Z. Ao, J. Liu, H. Sun, A.I. Rykov, J. Wang, Topotactic transformation of metal-organic frameworks to graphene-encapsulated transition-metal nitrides as efficient Fenton-like catalysts, *ACS Nano* 10 (2016) 11532–11540.
- [14] L. Lai, H. Ji, H. Zhang, R. Liu, C. Zhou, W. Liu, Z. Ao, N. Li, C. Liu, G. Yang, B. Lai, Activation of peroxydisulfate by V-Fe concentrate ore for enhanced degradation of carbamazepine: surface =V(III) and =V(IV) as electron donors promoted the regeneration of =Fe(II), *Appl. Catal. B Environ.* 282 (2021) 119559–119572.
- [15] E.T. Yun, S.W. Park, H.J. Shin, H. Lee, D.W. Kim, J. Lee, Peroxymonosulfate activation by carbon-encapsulated metal nanoparticles: switching the primary reaction route and increasing chemical stability, *Appl. Catal. B Environ.* 279 (2020) 119360–119372.
- [16] B. Qiao, A. Wang, X. Yang, L.F. Allard, T. Zhang, Single-atom catalysis of CO oxidation using Pt1/FeOx, *Nat. Chem.* 3 (2011) 634–641.
- [17] T. Sun, S. Mitchell, J. Li, P. Lyu, X. Wu, J. Pérez-Ramírez, Design of local atomic environments in single-atom electrocatalysts for renewable energy conversions, *Adv. Mater.* (2020) 2003075–2003104.
- [18] Y. Lu, Z. Zhang, H. Wang, Y. Wang, Toward efficient single-atom catalysts for renewable fuels and chemicals production from biomass and CO₂, *Appl. Catal. B Environ.* 292 (2021) 120162–120199.
- [19] Y. Shang, X. Xu, B. Gao, S. Wang, X. Duan, Single-atom catalysis in advanced oxidation processes for environmental remediation, *Chem. Soc. Rev.* 50 (2021) 5281–5322.
- [20] B. Huang, Z. Wu, H. Zhou, J. Li, C. Zhou, Z. Xiong, Z. Pan, G. Yao, B. Lai, Recent advances in single-atom catalysts for advanced oxidation processes in water purification, *J. Hazard. Mater.* 412 (2021) 125253–125273.
- [21] Y. Peng, B. Lu, S. Chen, Carbon-supported single atom catalysts for electrochemical energy conversion and storage, *Adv. Mater.* 30 (2018) 1801995–1802019.
- [22] J. Leverett, R. Daiyan, L. Gong, K. Iputera, Z. Tong, J. Qu, Z. Ma, Q. Zhang, S. Cheong, J. Cairney, R. Liu, X. Lu, Z. Xia, L. Dai, R. Amal, Designing undercoordinated Ni-Nx and Fe-Nx on holey graphene for electrochemical CO₂ conversion to syngas, *ACS Nano* (2021), <https://doi.org/10.1021/acsnano.1c03293>.
- [23] X. Li, X. Huang, S. Xi, S. Miao, J. Ding, W. Cai, S. Liu, X. Yang, H. Yang, J. Gao, J. Wang, Y. Huang, T. Zhang, B. Liu, Single cobalt atoms anchored on porous N-doped graphene with dual reaction sites for efficient Fenton-like catalysis, *J. Am. Chem. Soc.* 140 (2018) 12469–12475.
- [24] X. Mi, P. Wang, S. Xu, L. Su, H. Zhong, H. Wang, Y. Li, S. Zhan, Almost 100% peroxymonosulfate conversion to singlet oxygen on single-atom CoN₂₊₂ sites, *Angew. Chem. Int. Ed.* 60 (2020) 4588–4593.
- [25] H. Xu, N. Jiang, D. Wang, L. Wang, Y. Song, Z. Chen, J. Ma, T. Zhang, Improving PMS oxidation of organic pollutants by single cobalt atom catalyst through hybrid radical and non-radical pathways, *Appl. Catal. B Environ.* 263 (2020) 118350–118356.
- [26] Y. Gao, Y. Zhu, T. Li, Z. Chen, Q. Jiang, Z. Zhao, X. Liang, C. Hu, Unraveling the high-activity origin of single-atom iron catalysts for organic pollutant oxidation via peroxymonosulfate activation, *Environ. Sci. Technol.* 55 (2021) 8318–8328.
- [27] L. Peng, X. Duan, Y. Shang, B. Gao, X. Xu, Engineered carbon supported single iron atom sites and iron clusters from Fe-rich Enteromorpha for Fenton-like reactions via nonradical pathways, *Appl. Catal. B Environ.* 287 (2021) 119963–119974.
- [28] K. Qian, H. Chen, W. Li, Z. Ao, Y.N. Wu, X. Guan, Single-atom Fe catalyst outperforms its homogeneous counterpart for activating peroxymonosulfate to achieve effective degradation of organic contaminants, *Environ. Sci. Technol.* 55 (2021) 7034–7043.
- [29] S. Zuo, X. Jin, X. Wang, Y. Lu, Q. Zhou, J. Wang, W. Liu, Y. Du, J. Wang, Sandwich structure stabilized atomic Fe catalyst for highly efficient Fenton-like reaction at all pH values, *Appl. Catal. B Environ.* 282 (2021) 119551–119557.
- [30] J. Yang, D. Zeng, Q. Zhang, R. Cui, M. Hassan, L. Dong, J. Li, Y. He, Single Mn atom anchored on N-doped porous carbon as highly efficient Fenton-like catalyst for the degradation of organic contaminants, *Appl. Catal. B Environ.* 279 (2020) 119363–119972.
- [31] J. Miao, Y. Zhu, J. Lang, J. Zhang, S. Cheng, B. Zhou, L. Zhang, P.J.J. Alvarez, M. Long, Spin-state-dependent peroxymonosulfate activation of single-atom M-N moieties via a radical-free pathway, *ACS Catal.* 11 (2021) 9569–9577.
- [32] X. Wang, Z. Chen, X. Zhao, T. Yao, W. Chen, R. You, C. Zhao, G. Wu, J. Wang, W. Huang, J. Yang, X. Hong, S. Wei, Y. Wu, Y. Li, Regulation of coordination number over single Co sites: Triggering the efficient electroreduction of CO₂, *Angew. Chem. Int. Ed.* 130 (2018) 1962–1966.
- [33] Y. Zhang, L. Jiao, W. Yang, C. Xie, H. Jiang, Rational fabrication of low-coordinate single-atom Ni electrocatalysts by MOFs for highly selective CO₂ reduction, *Angew. Chem. Int. Ed.* 60 (2021) 1–6.
- [34] Y. Gao, Y. Zhu, L. Lyu, Q. Zeng, X. Xing, C. Hu, Electronic structure modulation of graphitic carbon nitride by oxygen doping for enhanced catalytic degradation of organic pollutants through peroxymonosulfate activation, *Environ. Sci. Technol.* 52 (2018) 14371–14380.
- [35] H. Zhou, H. Zhang, Y. He, B. Huang, C. Zhou, G. Yao, B. Lai, Critical review of reductant-enhanced peroxide activation processes: trade-off between accelerated Fe³⁺/Fe²⁺ cycle and quenching reactions, *Appl. Catal. B Environ.* 286 (2021) 119900–119919.
- [36] Y. Gao, Y. Zhu, Z. Chen, Q. Zeng, C. Hu, Insights into the difference in metal-free activation of peroxymonosulfate and peroxydisulfate, *Chem. Eng. J.* 394 (2020) 123936–123946.
- [37] C. Liang, C.F. Huang, N. Mohanty, R.M. Kurakalva, A rapid spectrophotometric determination of persulfate anion in ISCO, *Chemosphere* 73 (2008) 1540–1543.
- [38] G. Kresse, J. Furthmüller, Efficient iterative schemes for ab initio total-energy calculations using a plane-wave basis set, *Phys. Rev. B* 54 (1996) 169–186.
- [39] J.P. Perdew, K. Burke, M. Ernzerhof, Generalized gradient approximation made simple, *Phys. Rev. Lett.* 77 (1996) 3865–3868.
- [40] Y. Gao, Y. Zhu, Z. Chen, C. Hu, Nitrogen-coordinated cobalt embedded in a hollow carbon polyhedron for superior catalytic oxidation of organic contaminants with peroxymonosulfate, *ACS EST Eng.* 1 (2020) 76–85.
- [41] Y. Gao, Z. Chen, Y. Zhu, T. Li, C. Hu, New insights into the generation of singlet oxygen in the metal-free peroxymonosulfate activation process: important role of electron-deficient carbon atoms, *Environ. Sci. Technol.* 54 (2020) 1232–1241.
- [42] L. Zhao, Y. Zhang, L. Huang, X. Liu, Q. Zhang, C. He, Z. Wu, L. Zhang, J. Wu, W. Yang, L. Gu, J. Hu, L. Wan, Cascade anchoring strategy for general mass production of high-loading single-atomic metal-nitrogen catalysts, *Nat. Commun.* 10 (2019) 1278–1288.
- [43] Y. Guo, P. Yuan, J. Zhang, Y. Hu, I.S. Amiinu, X. Wang, J. Zhou, H. Xia, Z. Song, Q. Xu, S. Mu, Carbon nanosheets containing discrete Co-Nx-By-C active sites for efficient oxygen electrocatalysis and rechargeable Zn-Air batteries, *ACS Nano* 12 (2018) 1894–1901.
- [44] W.D. Oh, Z. Dong, T.T. Lim, Generation of sulfate radical through heterogeneous catalysis for organic contaminants removal: current development, challenges and prospects, *Appl. Catal. B Environ.* 194 (2016) 169–201.
- [45] S. Liu, D. Li, H. Sun, H.M. Ang, M. Tadé, S. Wang, Oxygen functional groups in graphitic carbon nitride for enhanced photocatalysis, *J. Colloid Interface Sci.* 468 (2016) 176–182.

[46] Y. Gao, Y. Li, L. Yao, S. Li, J. Liu, H. Zhang, Catalyst-free activation of peroxides under visible LED light irradiation through photoexcitation pathway, *J. Hazard. Mater.* 329 (2017) 272–279.

[47] K.J.G.S.L. Timmins, E.J.H. Bechara, Y. Kotake, H.M. Swartz, Trapping of free radicals with direct in vivo EPR detection: a comparison of 5,5-dimethyl-1-pyrroline-N-oxide and 5-diethoxyphosphoryl-5-methyl-1-pyrroline-N-oxide as spin traps for •OH and SO₄^{•-}, *Free Radic. Biol. Med.* 27 (1999) 329–333.

[48] Z. Chen, T. Li, Y. Zhu, X. Liang, Z. Zhao, D. Wang, J. Li, Y. Gao, C. Hu, Efficient light-free activation of peroxyomonosulfate by carbon ring conjugated carbon nitride for elimination of organic pollutants, *Chem. Eng. J.* 420 (2021) 129671–129682.

[49] Y. Wang, G. Jia, X. Cui, X. Zhao, Q. Zhang, L. Gu, L. Zheng, L. Li, Q. Wu, D.J. Singh, D. Matsumura, T. Tsuji, Y. Cui, J. Zhao, W. Zheng, Coordination number regulation of molybdenum single-atom nanozyme peroxidase-like specificity, *Chem* 7 (2021) 1–14.

[50] Y. Li, J. Li, J. Huang, J. Chen, Y. Kong, B. Yang, Z. Li, L. Lei, G. Chai, Z. Wen, L. Dai, Y. Hou, Boosting electroreduction kinetics of nitrogen to ammonia via tuning electron distribution of single-atomic iron sites, *Angew. Chem. Int. Ed.* 60 (2021) 9078–9085.

[51] X. Ge, S.S. Yu, R.F. Cheng, W. Chen, F. Zhou, K. Liang, J.J. Chen, H.Q. Yu, Y. Wu, Controllable drilling by corrosive Cu₁O_x to access highly accessible single-site catalysts for bacterial disinfection, *Appl. Catal. B Environ.* 293 (2021) 120228–120235.

[52] G. Wang, S. Chen, Q. Xie, H. Yu, Y. Zhang, Enhanced activation of peroxyomonosulfate by nitrogen doped porous carbon for effective removal of organic pollutants, *Carbon* 115 (2017) 730–739.